Supporting Information

Photo modulated Fluidic Channels for Precise Delivery of Ions and Molecules

Kiran Mayawad[a], Sonali Roy[a], Bipasha Saikia[a], Dibakar Das[a], Kalyan Raidongia [a]*
[a]*Department of Chemistry, Indian Institute of Technology Guwahati, Guwahati, Assam 781039, India.*

Contents

1. **Experimental methods:**

1.1 Device fabrication: The required membrane was cut into different geometries and embedded within a polydimethylsiloxane (PDMS) matrix. The polymer was allowed to cure at room temperature for 12 h. After curing, two reservoirs adjacent to the membrane were carved into the device and filled with electrolyte solutions as depicted for a triangular membrane piece in Figure S1.

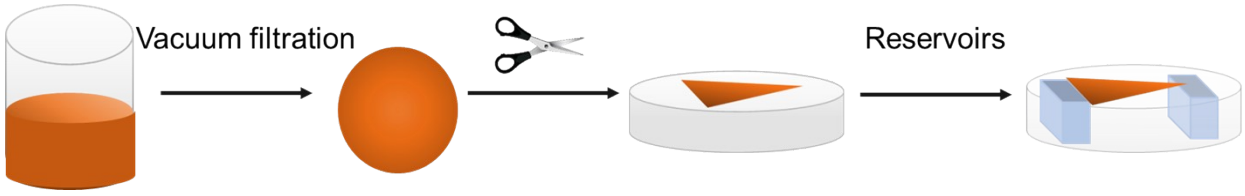

Figure S1: Schematic representation for device fabrication steps

Dimensions of membranes used for fabricating fluidic devices of different geometries are described below:

- **HFM (VO-o-CNT bilayer):**

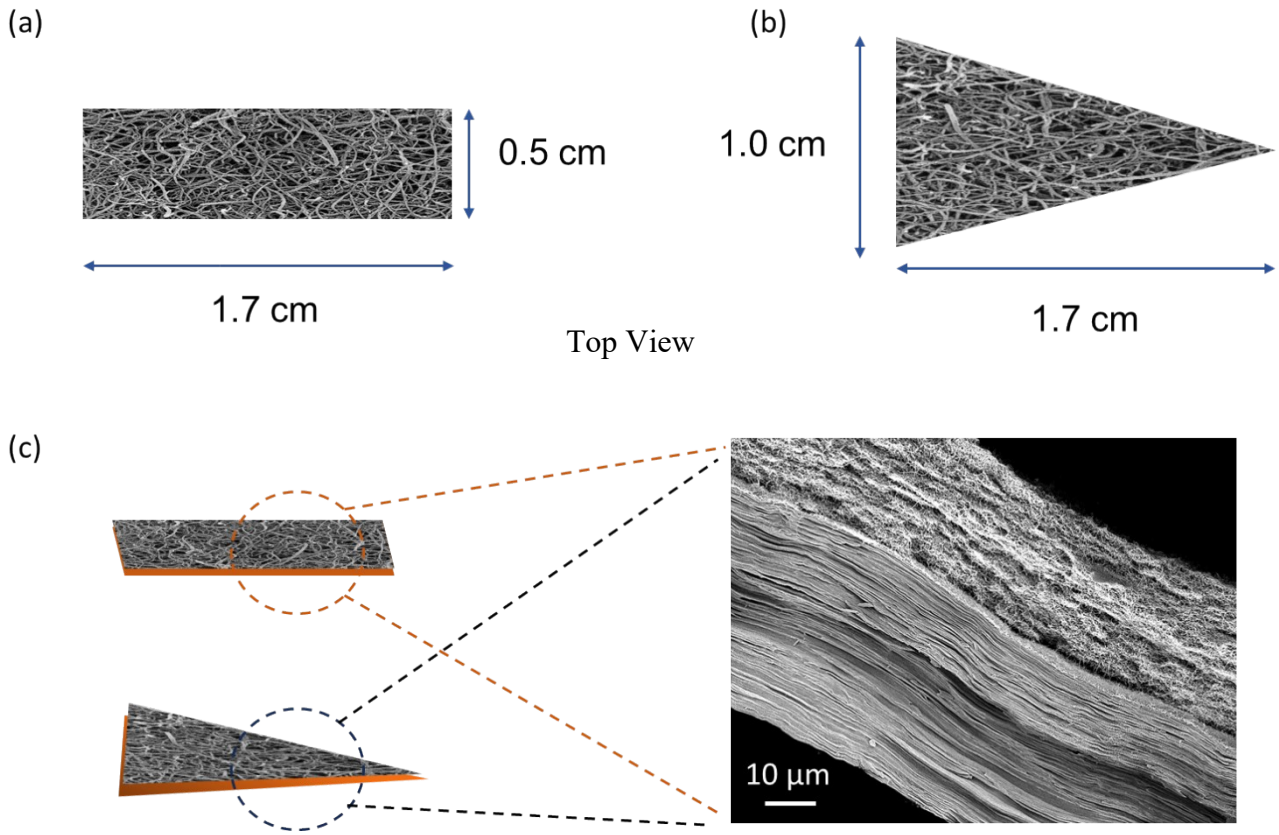

Figure S1.1: VO-o-CNT heterostructure fluidic membrane (HFM), top view of (a) rectangular strip and (b) triangular strip with dimensions, (c) Schematic of the lateral view with cross sectional FESEM image of the rectangular and triangular strips.

- **IFM (VO and o-CNT) device:**

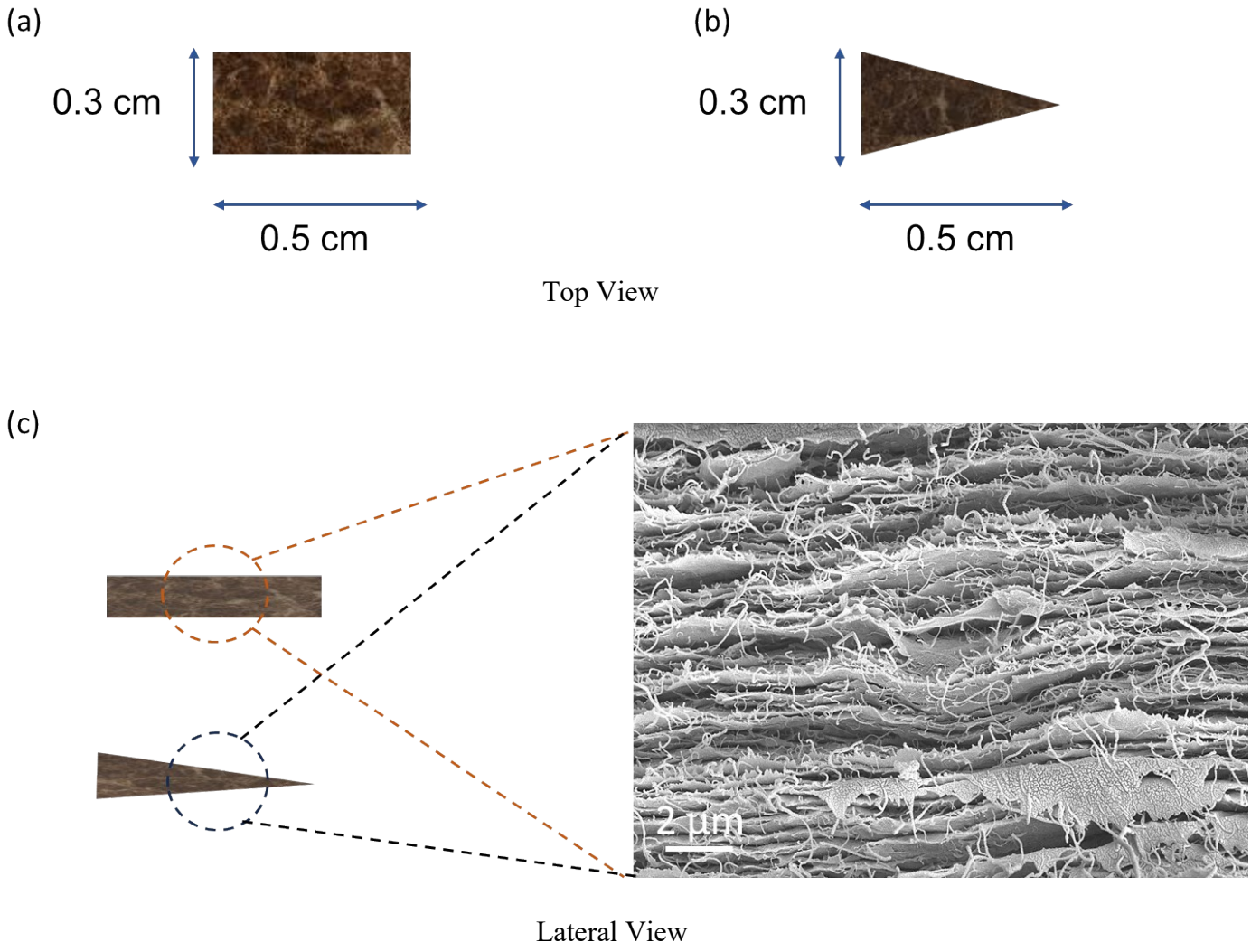

Figure S1.2: VO and o-CNT intermixed fluidic membrane (IFM), Schematic illustration of (a) the top view of rectangular strip and (b) triangular strip with dimensions, and (b) lateral view with FESEM cross sectional image of the rectangular and triangular strips.

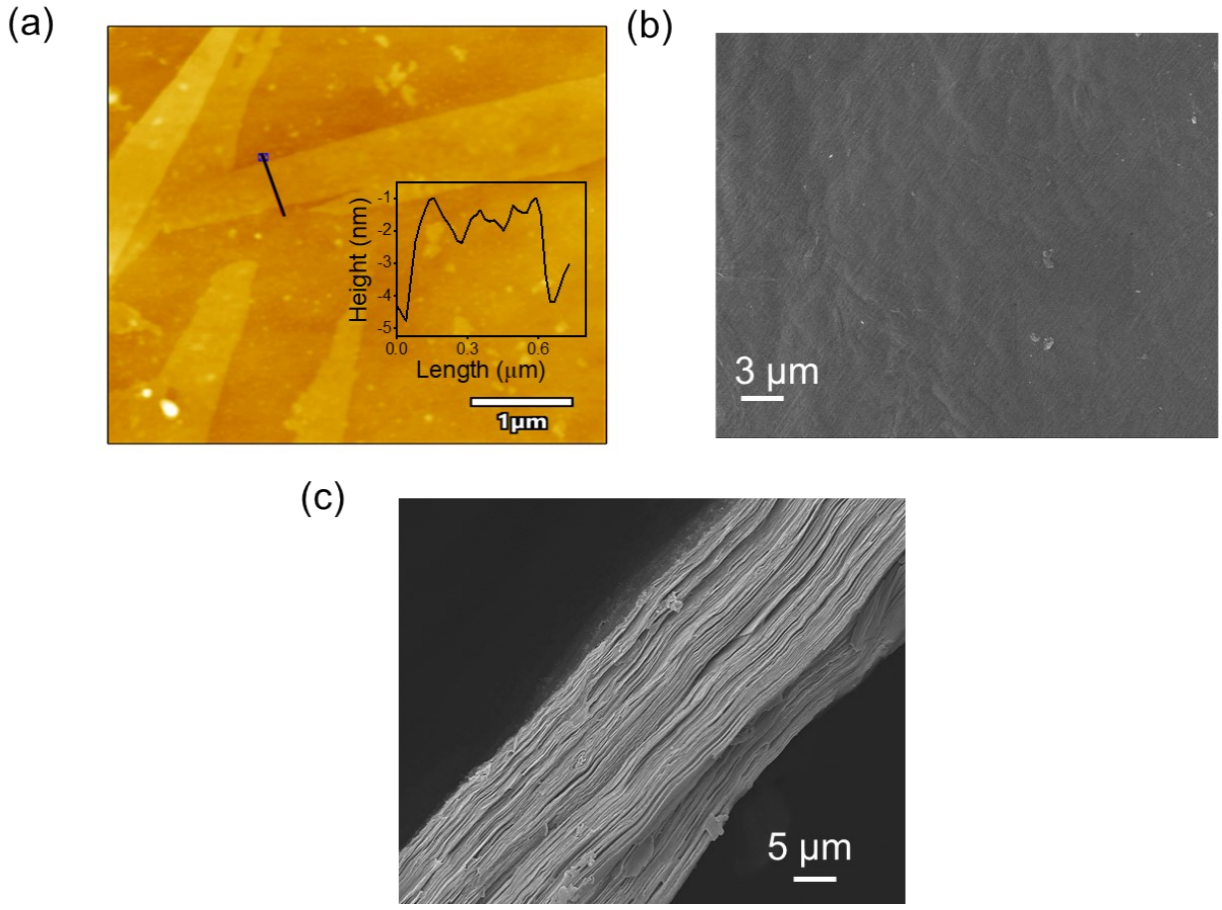

Figure S2: (a) AFM image along with the corresponding height profile of VO nanosheets. (b) FESEM image illustrating surface morphology of VO membrane. (c) Cross sectional FESEM image of VO membrane.

2 Supporting figures for characterization:

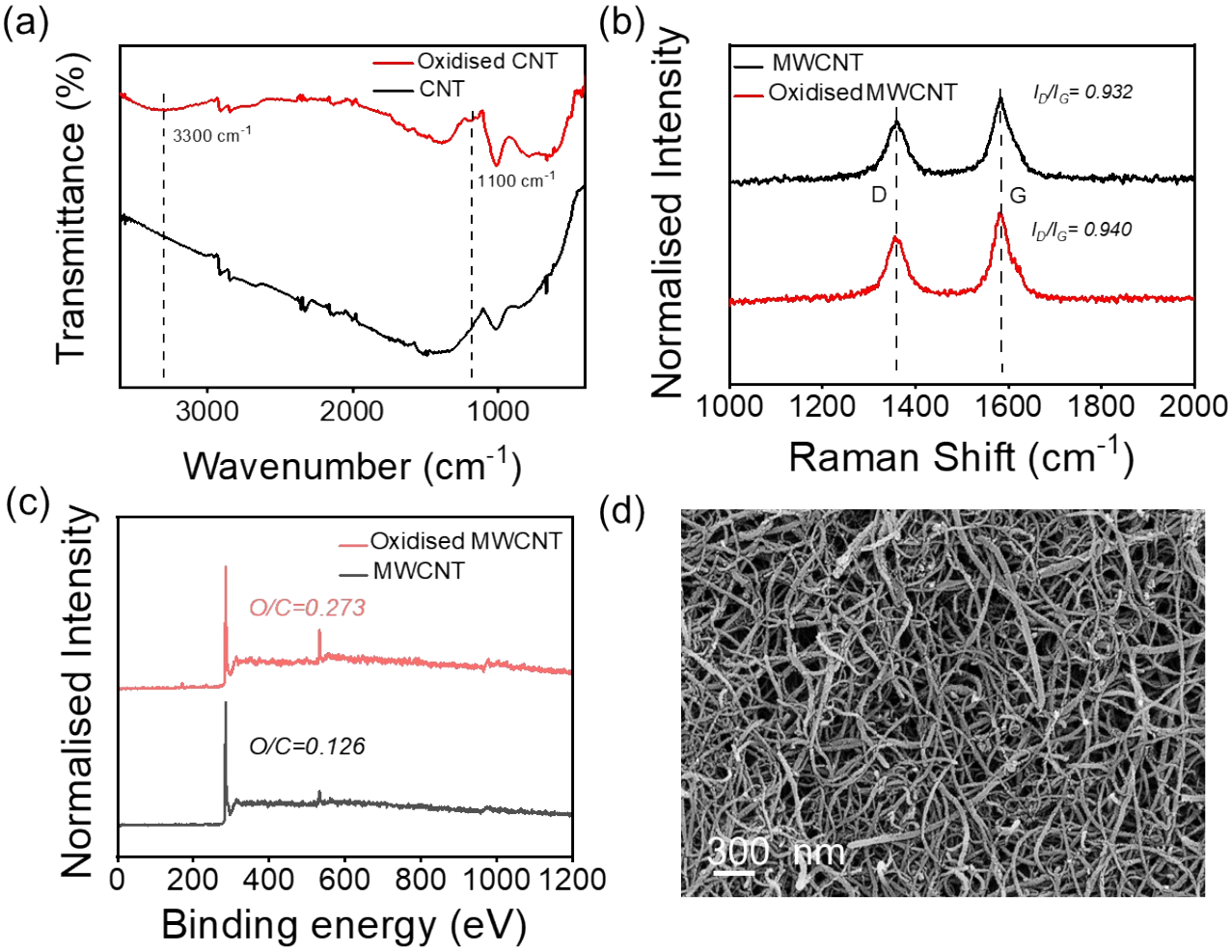

Figure S3: Characterisation of o-CNT membrane: (a) FTIR spectra of CNT and o-CNT, exhibiting new peaks at 1100 and 3300 cm^{-1} arising due to oxidation (b) RAMAN spectra showing increased I_D/I_G ratio of o-CNT due to functionalization. (c) XPS plot of o-CNT and CNT depicting higher O/C ratio of oxidised CNT than that of the pristine CNTs. (d) FESEM and (e) AFM image showing fibrous morphology of oCNTs.

3 Calculations:

3.1 Determination of photothermal conversion efficiency: (η)

The photothermal conversion efficiency (η) was calculated using the formula mentioned below:

$$\eta = Q/E = (cm\Delta T)/pst$$

Here, Q denotes the thermal energy produced by the absorber, while E corresponds to the total energy of the incident light. The parameters c and m represent the specific heat capacity and mass of the photothermal material, respectively. ΔT indicates the temperature rise under light exposure, p refers to the power density of the light source, and s and t denote the irradiated area and duration of exposure.

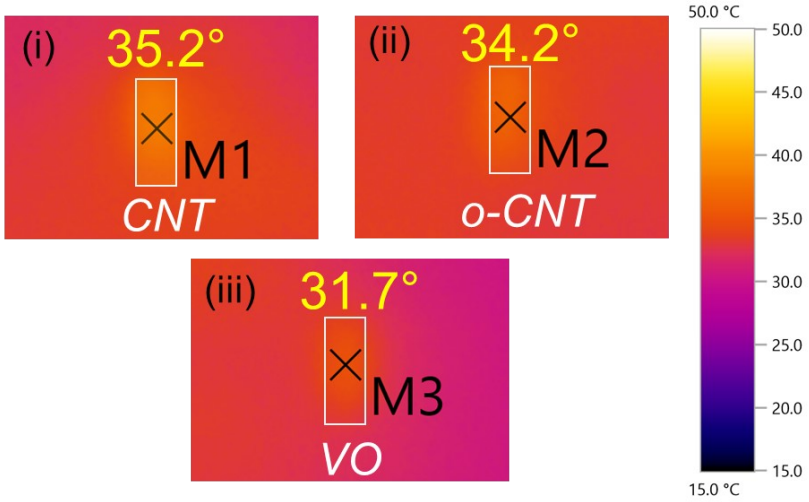

3.2 Determination of transport number:

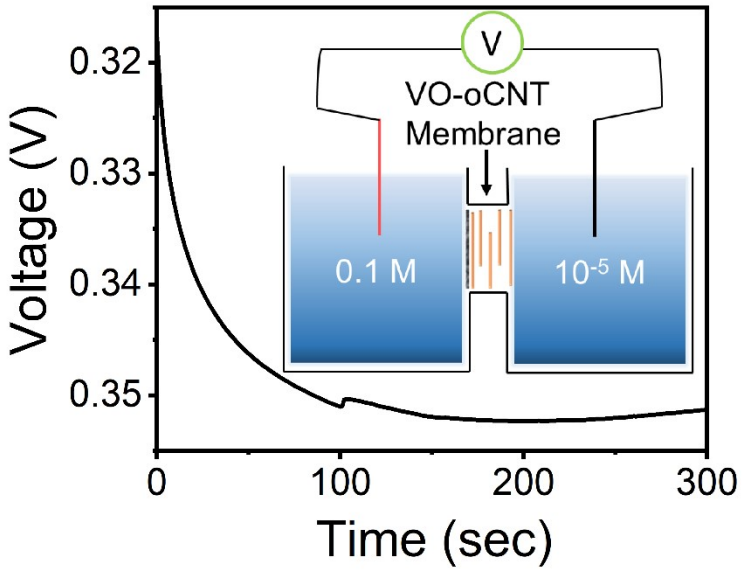

Figure S5: Voltage vs time plot obtained with HFM under a 10^4 - fold concentration gradient of KCl. The transport number was calculated to be ~ 0.8, from the potential drop at 300 sec.

The transport number of the HFM membrane was determined by recording the potential difference across electrolyte solutions with different concentrations (10^{-1} and 10^{-5} M KCl). The transport number of cations were calculated by using the equation 1 given below:

$$E_J = V_{obs.} - V_{redox} = (2t_c - 1) \times \frac{RT}{F} \ln c1/c2 \quad \ldots\ldots\ldots (1)$$

Here, E_J denotes the junction potential, V_{obs} is the observed potential across the membrane, and V_{redox} represents the potential drop arising from redox processes at the electrode–electrolyte interface. t_c corresponds to the cation transport number, R is the universal gas constant, T is the absolute temperature, F is the Faraday constant, and c_1 and c_2 represent the higher and lower electrolyte concentrations, respectively.

Here, V_{redox} refers to the Nernst potential generated at the electrode–electrolyte interface as a result of unequal chloride concentrations in the reservoirs. The values employed were theoretically calculated using the Nernst equation (Equation 2) for different concentration gradients.

$$V_{redox} = \frac{k_B T}{q_{ion}} \ln c1/c2 \qquad \ldots\ldots\ldots\ldots (2)$$

Here, k_B denotes the Boltzmann constant, T is the absolute temperature (K), q_{ion} is the charge of the migrating ion, and c_1 and c_2 represent the higher and lower electrolyte concentrations, respectively.

3.3 Determination of ion delivery rate from *I-t* curve:

The ion delivery rate was derived from the I–t curve by considering the current values as indicative of the number of ions moving from the higher-concentration region to the lower-concentration side of the fluidic triangle. The average ion transport rate across the membrane was then obtained by integrating the I–t curve and dividing the resulting area by the time interval $(t_2 - t_1)$.

$$Average\ current = \frac{Area\ under\ curve}{Time\ difference\ (t_2 - t_1)}$$

From the average current value, the rate of ion transport through the nanochannels was calculated as follows:

Since 1 ampere corresponds to 1 coulomb of charge per second, and the charge on a single ion is 1.6×10^{-19} C, let the average current obtained from the area under the I–t curve be x_A.

The number of ions corresponding to a charge of xC/s is:

$$\frac{x \text{ C/s}}{1.6 \times 10^{-19} \text{ C/ion}}$$

Therefore, the characteristic ion transport rate is:

$$\frac{x}{1.6 \times 10^{-19}} \text{ ions/s}$$

This value is then converted to mol/min using:

$$\text{Delivery rate} = \frac{(\text{Average area}) \times 60}{1.6 \times 10^{-19} \times 6.022 \times 10^{23}} \text{ mol/min}$$

3.4 Determination of conductivity of drain reservoir:

To measure conductivity in the drain reservoir, *I–V* curves were recorded at regular time intervals through two Ag/AgCl electrodes, positioned approximately 0.4 cm apart inside the drain reservoir. The conductivity was determined by normalizing the slope of each *I–V* curve with respect to the electrode separation and the cross-sectional area of the reservoir.

3.5 Determination of channel height:

The average channel height (h_{eff}) was determined by utilizing the equation mentioned below:

$$h_{eff} = \frac{\sigma \times 10^{-3}}{C_t N_A e}$$

where, σ is the surface charge density, N_A is the Avogadro's number, e is the electronic charge and C_t is the transition concentration. The transition concentration is determined from the surface charge governed ionic conductivity plot of the system (Figure S3). To calculate the surface charge density, the following equation is used:

$$\sigma = \frac{\varepsilon \varepsilon_0 \zeta}{\lambda_d}$$

Here, ε is the dielectric constant of water, ε_0 is the permittivity in vacuum, ζ is the zeta potential of the V_2O_5 and o-CNT intermixed (100:150) dispersion and λ_d is the Debye length of water.

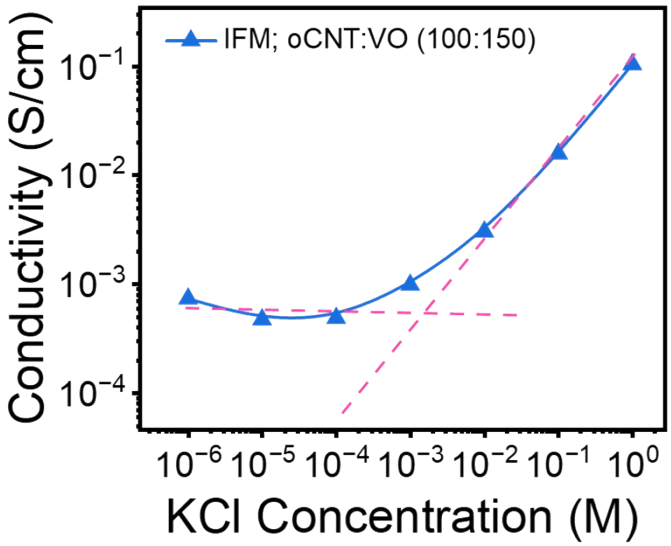

Figure S6: Determination of transition concentration (C_t) from the surface charge governed ionic conductivity plot for rectangular VO-o-CNT (IFM; o-CNT:VO ratio: 100:150).

4 Supporting figures and tables

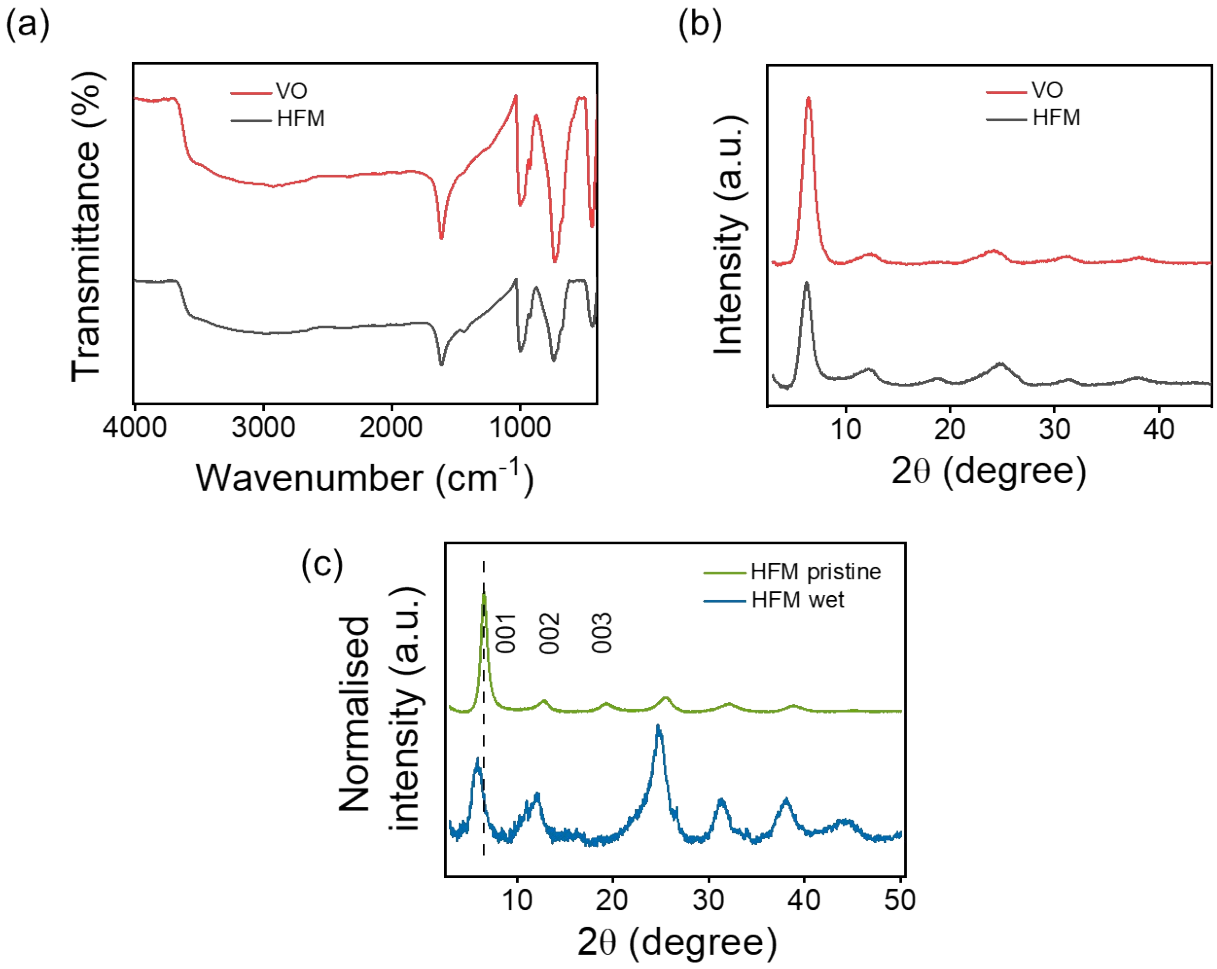

Figure S7: (a) FTIR spectra, and pXRD pattern of (b) VO and HFM. (c) XRD patterns of HFM in dry and wet states.

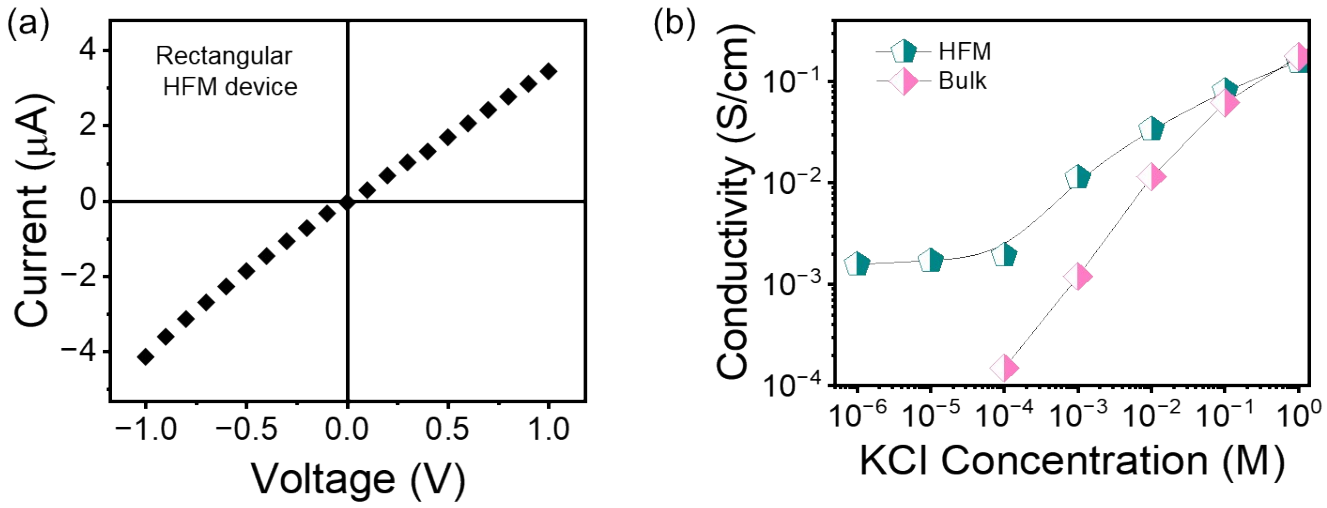

Figure S8: (a) Current vs voltage (*I-V*) plot of rectangular HFM device. (b) Conductivity vs KCl concentration plot of HFM device exhibiting characteristic surface charge governed ionic transport.

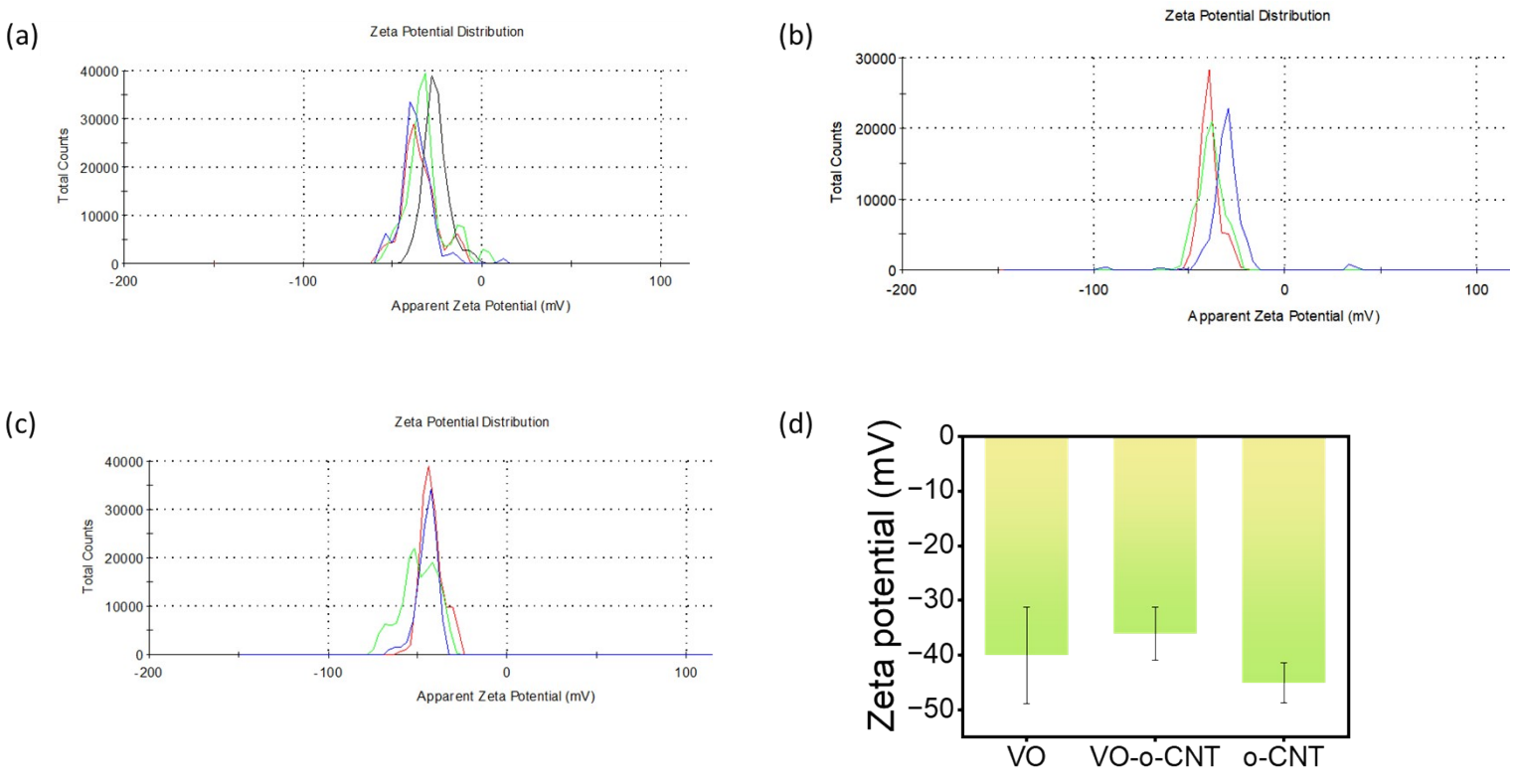

Figure S9: Zeta potential distribution plot for aqueous dispersion of (a) VO, (b) VO-o-CNT and (c) o-CNT, (d) a comparison plot for zeta potential for the dispersions.

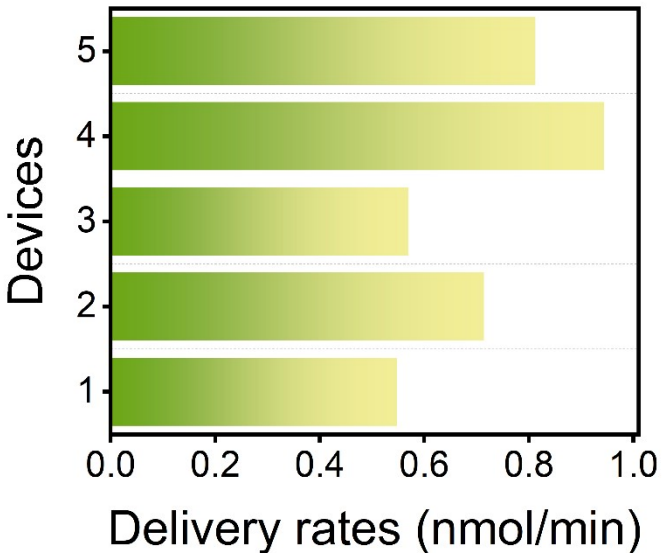

Figure S10: The observed ion delivery rates for five HFM devices in similar configurations (source with 10^{-1} M and drain with 10^{-5} M KCl solutions).

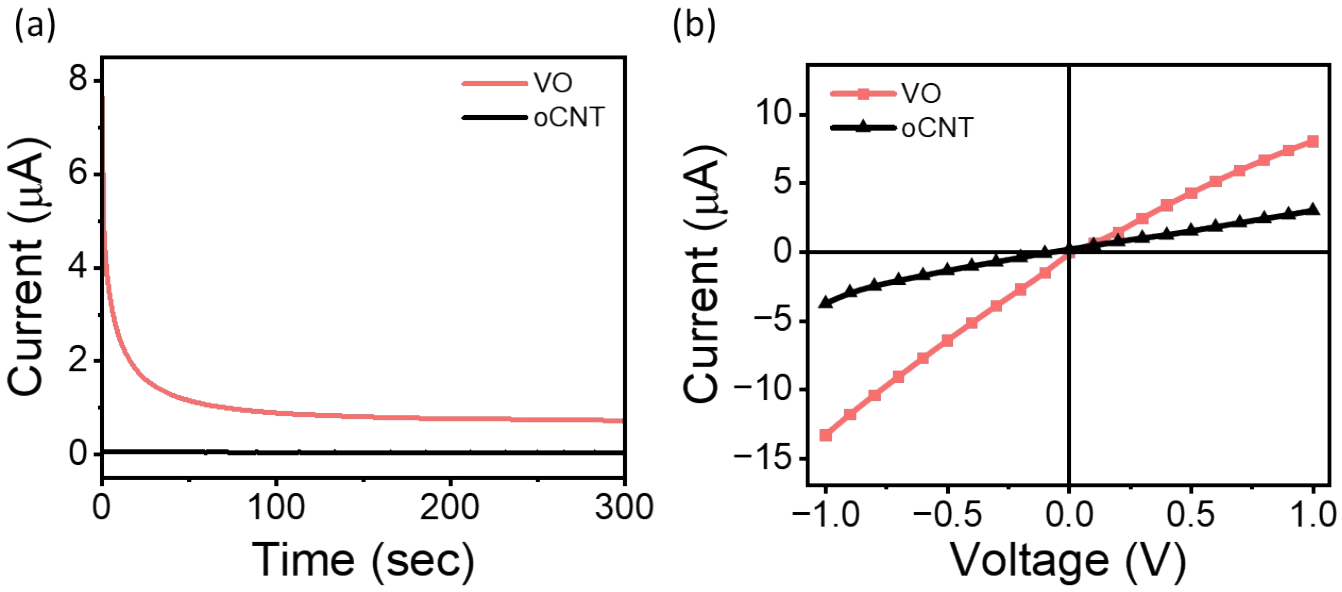

Figure S11: (a) Current vs time plot of triangular o-CNT membrane compared with that of triangular VO membrane (10^{-1} M KCl as source and 10^{-5} M KCl at drain). (b) I-V plot showing increment in ionic conductivity value inside the drain reservoir after 300 seconds.

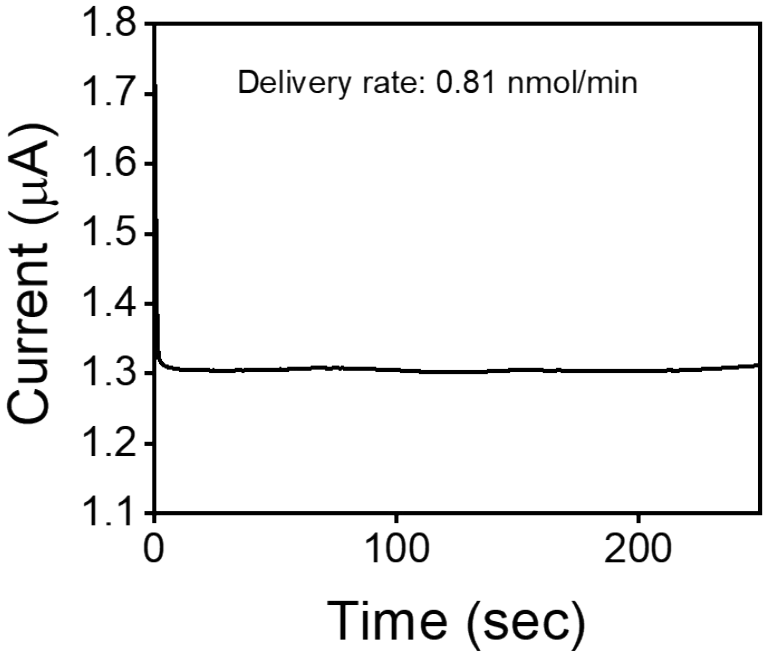

Figure S12: Current vs time plot of triangular HFM device with 10^{-1} M KCl at the base and DI water at the vertex of the triangular membrane.

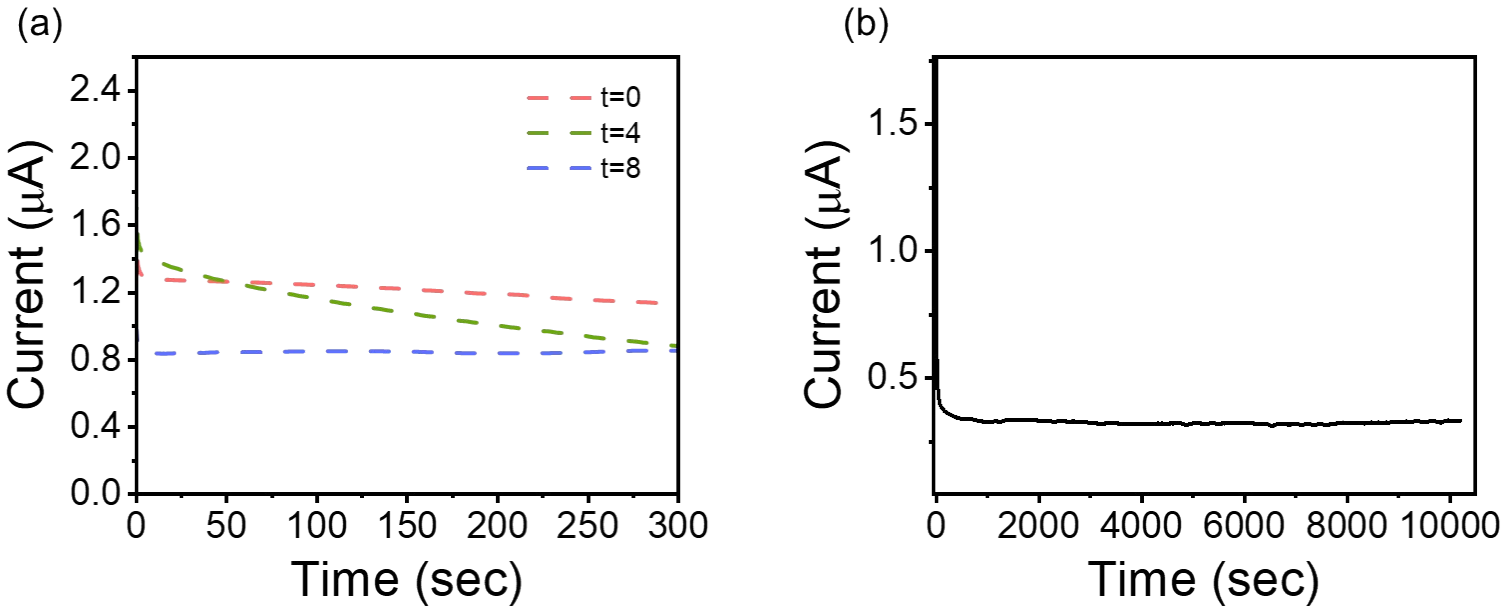

Figure S13: Current vs time (I-t) measurements, for a triangular HFM device under a 10^4 fold concentration gradient, with 0.1 M KCl placed at the base (source), (a) at a regular interval of time (4 hours), (b) for long term release of ions (10,000 seconds), exhibiting consistent release of potassium ions.

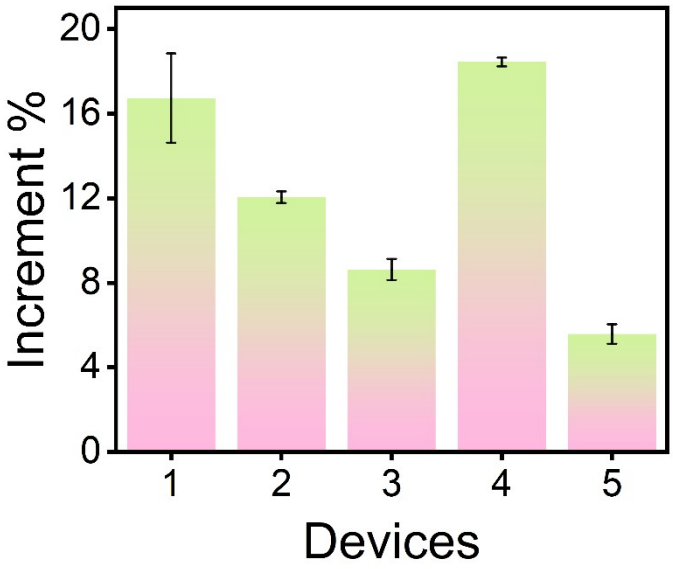

Figure S14: The increment percentage obtained from the area under *I-t* graph upon light illumination, plotted for five different HFM devices in similar device configuration.

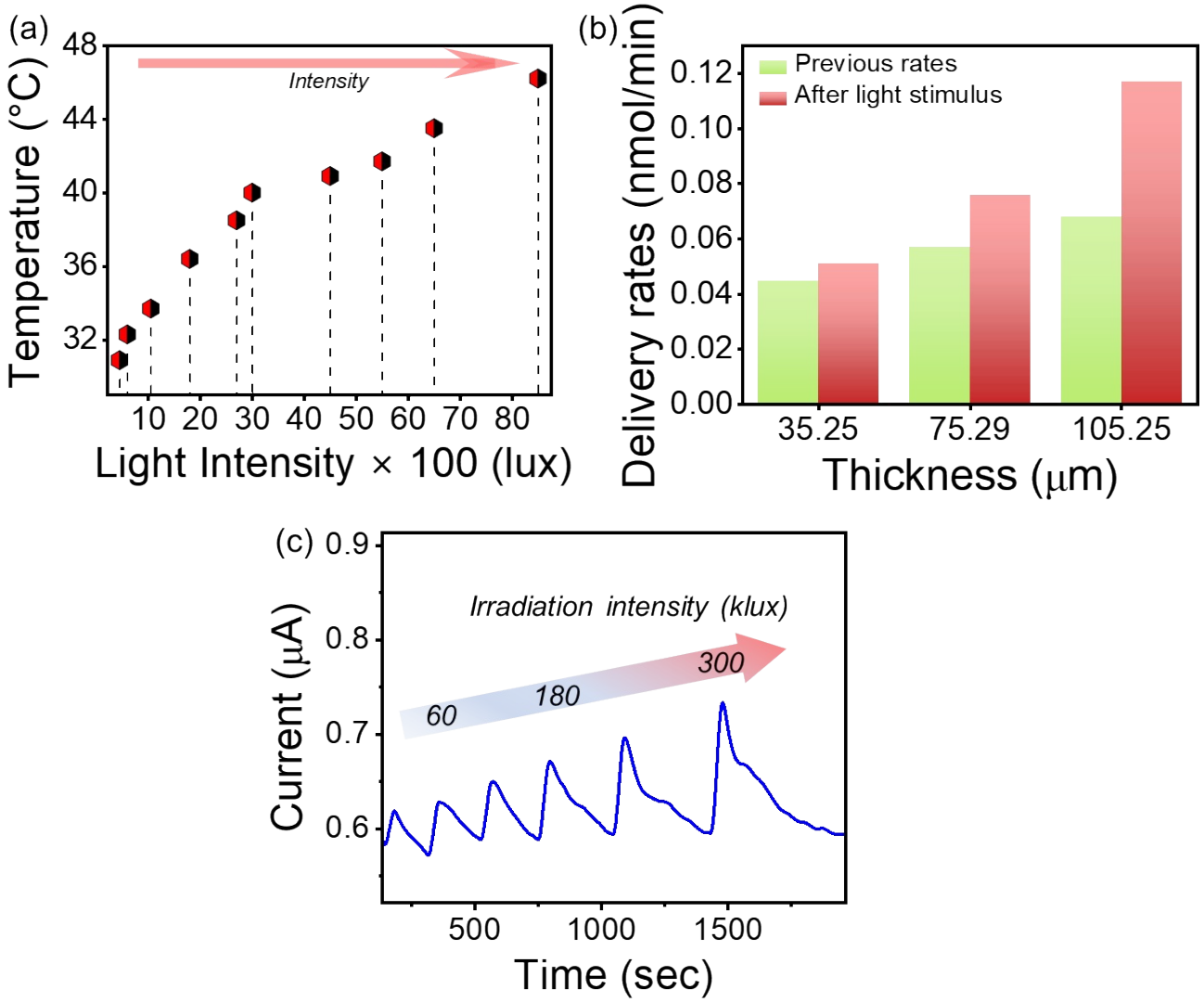

Figure S15: (a) The temperature variation of the triangular HFM device upon the intensity variation of the illuminated light. (b) Delivery rates obtained through ICP-MS analysis before and after light illumination for devices with varying thicknesses. (c) *I-t* plot demonstrating increasing current pulses upon increasing irradiated light intensity from 45 to 300 klux.

System	Stimulus	Transported ion/molecule	Transport metric	Rate/ratio/ percentage	Ref.

Table 1: A table comprising of a few stimuli-responsive ionic/molecular systems with their corresponding transport metrics and stimulus.

AAO membrane functionalised with ferrofluids	External magnetic field	Dodecyl trimethyl ammonium chloride (DTAC)molecules	Transport speed	0 -36.6 μgmL^{-1} min^{-1} (close to open state)	[1]
Hydrogel-based porous gating systems (HPGSs)	pH	Doxorubicin hydro chloride (DOX)	Colour change and concentration determination	1.47% to 72.80% in 48 hrs (pH>7)	[2]
Functionalised COF membrane	Light	Potassium ions	Transport rate	3.2×10^{12} ions/scm^2 Conc. Difference (2000:1)	[3]
Nanopores	Voltage	Ions	Rectification ratio	Over 40,000	[4]
GO membrane	Light	Ions	Transport rate	0.78 mol h^{-1} m^{-2}	[5]

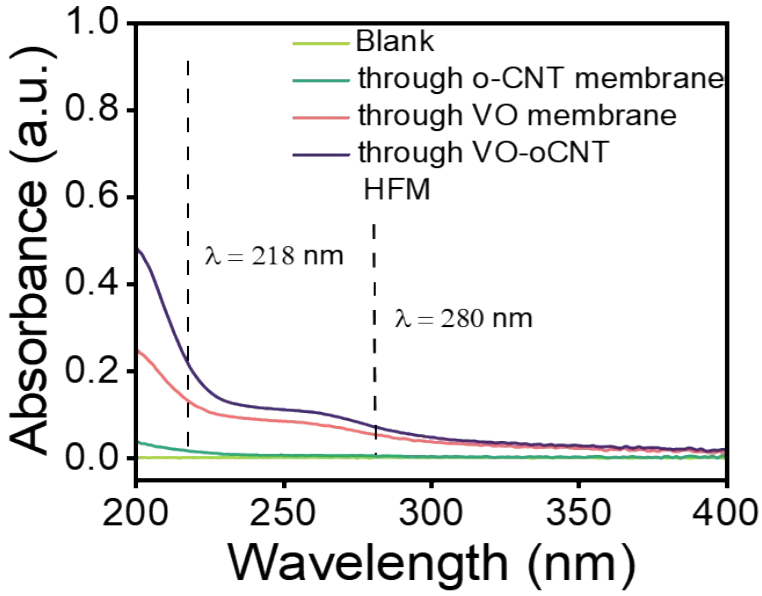

Figure S16: UV-vis plot demonstrating absence of Trp peaks (at 218 and 280 nm) in the molecular diffusion experiment through HFM, o-CNT, and VO membrane.

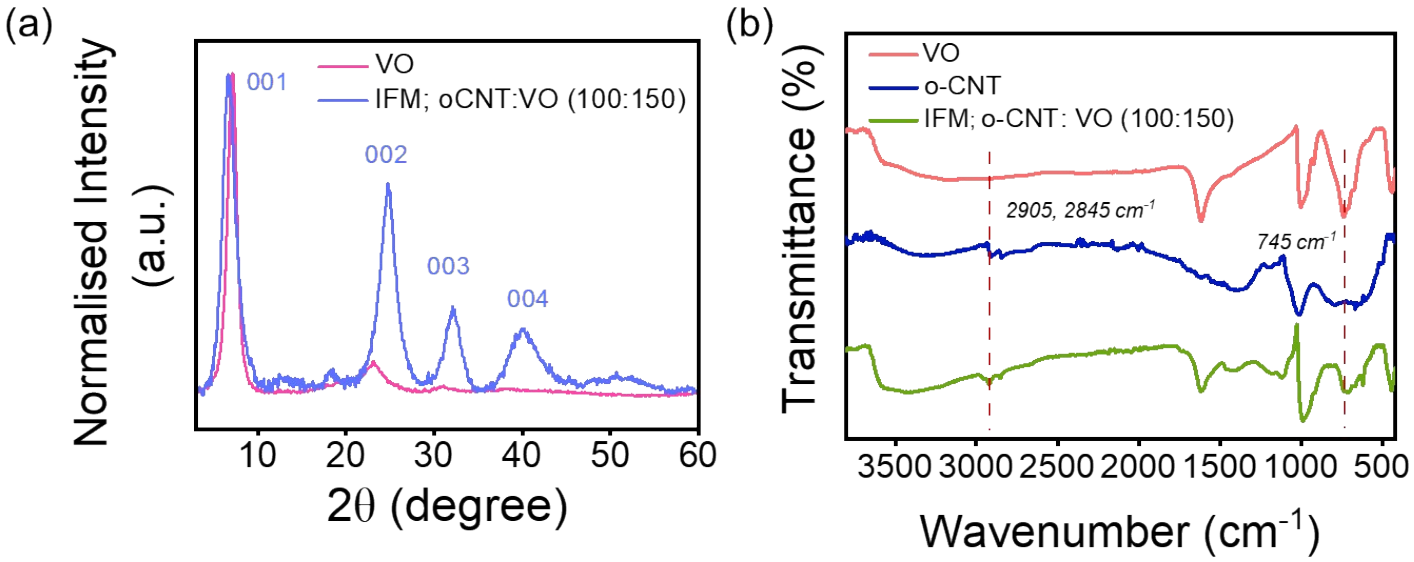

Figure S17: (a) pXRD pattern showing relative increase in the intensity of subordinate peaks of the IFM in comparison to that of VO, (b) FTIR spectra for IFM with VO and o-CNT exhibiting peaks corresponding to both the components.

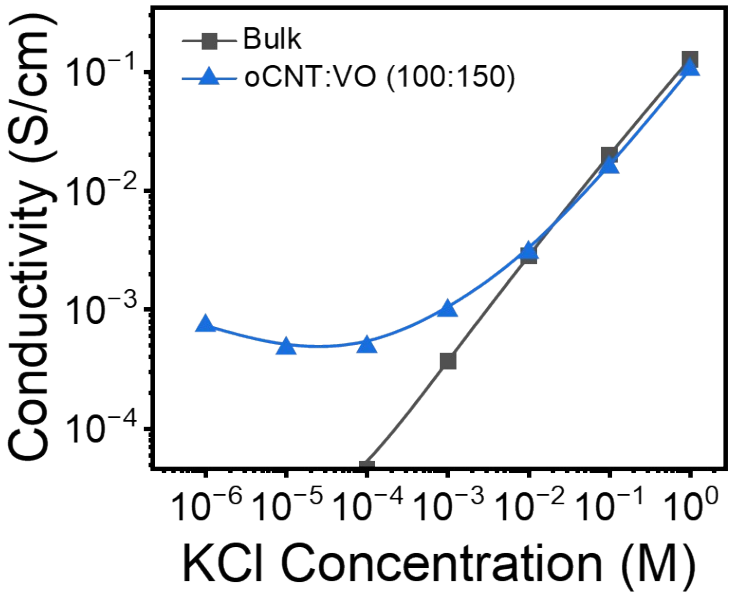

Figure S18: Characteristic surface charge governed ionic conductivity plot of the IFM (o-CNT : VO = 100:150).

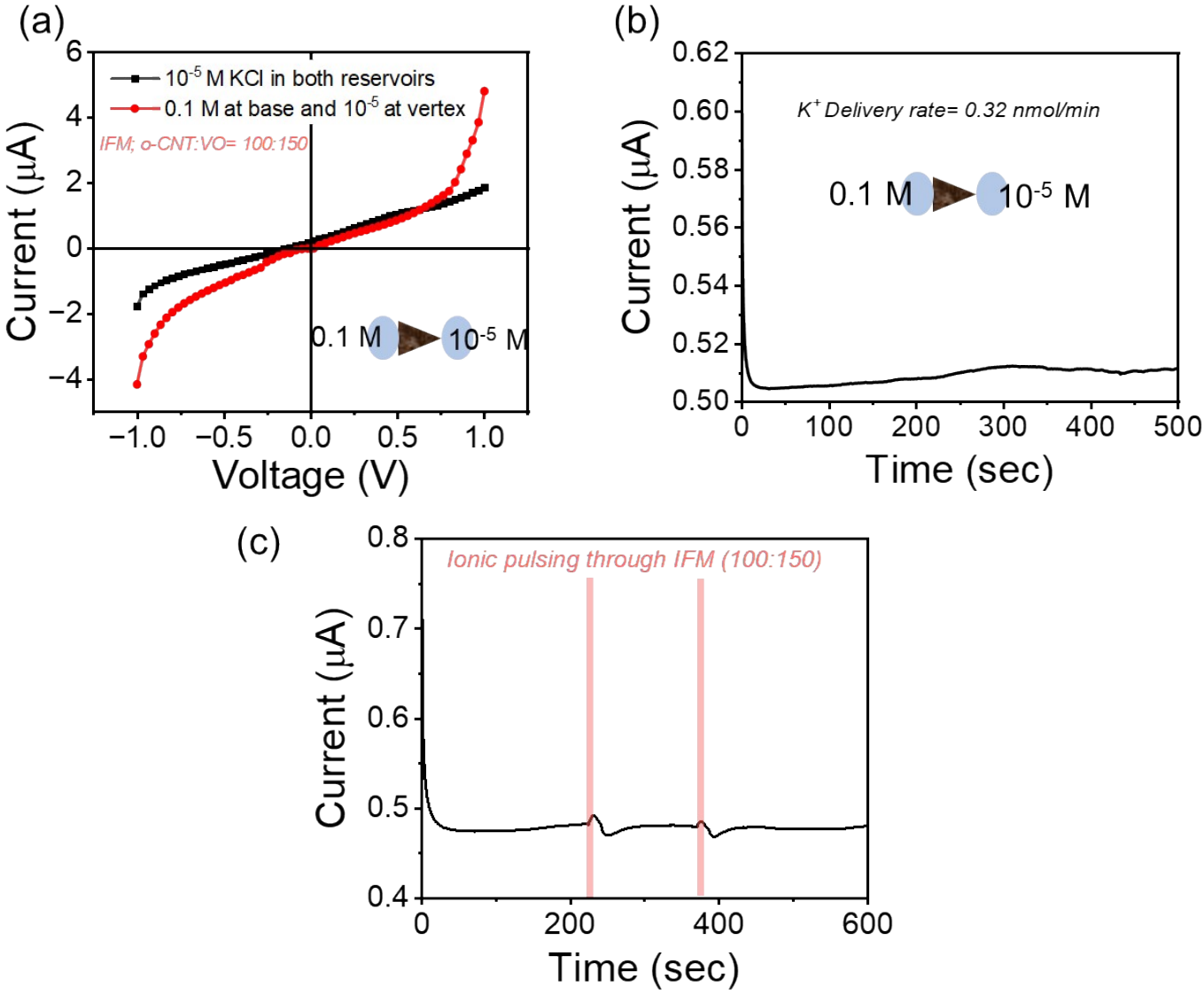

Figure S19: (a) I-V plot of triangular IFM with symmetrical (10^{-5} M KCl both sides) and asymmetrical electrolytes (0.1 M KCl at the base and 10^{-5} M KCl at the vertex) b) The current vs time plot of 100:150, o-CNT: VO triangular IFM with 0.1 M KCl as source and 10^{-5} M KCl as drain electrolyte. (c) The ionic pulsing through IFM device under light illumination (15 second pulses).

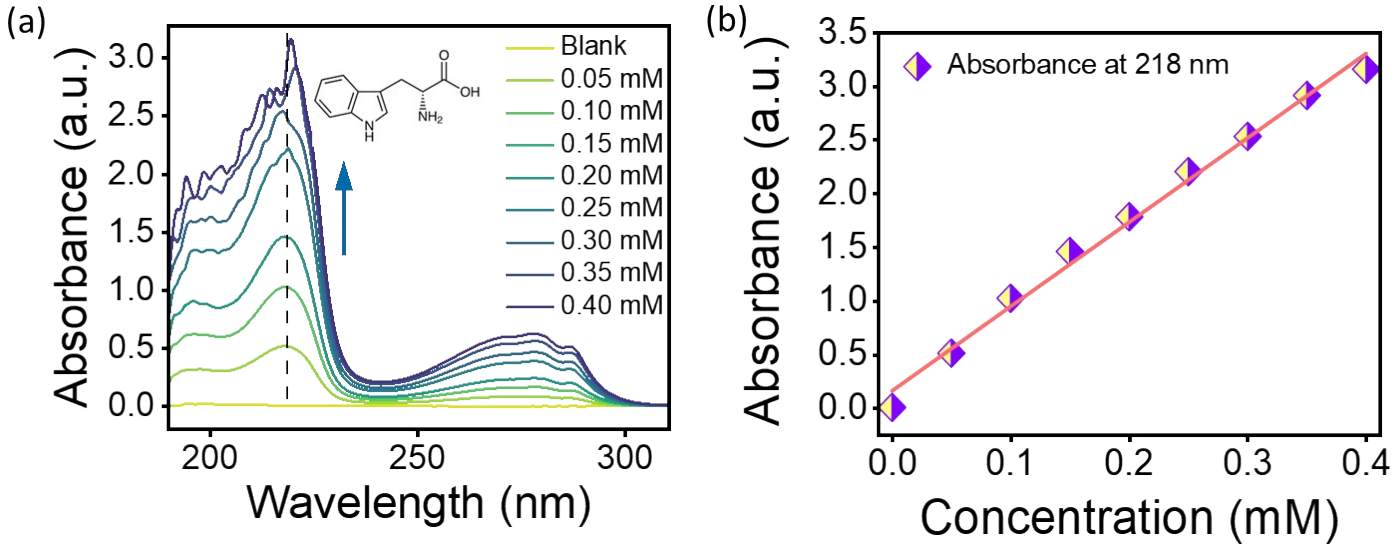

Figure S20: (a) UV-vis plot of Trp with increasing concentration. (b) the calibration curve of concentration with absorbance at 218 nm.

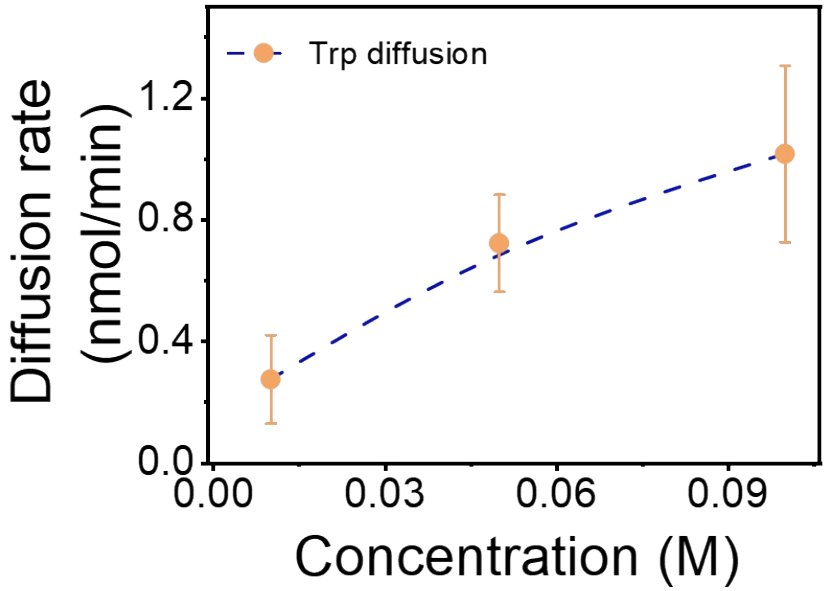

Figure S21: Variation of diffusion rate of Trp with increasing concentration.

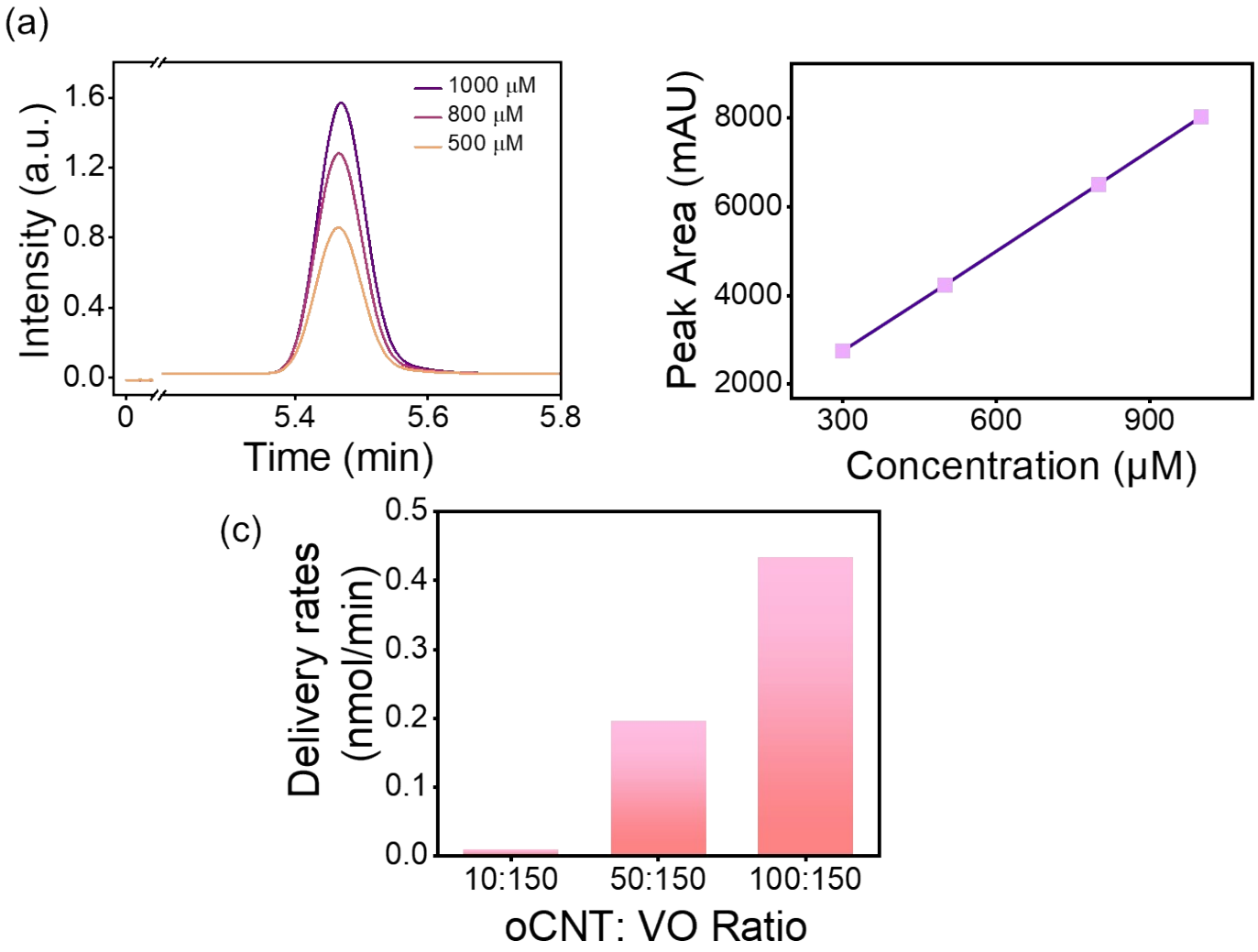

Figure S22: (a) HPLC peak, and (b) area under the peak of Trp at different concentrations**.** (c) Delivery rates of Trp calculated from HPLC analysis through IFM of different compositions.

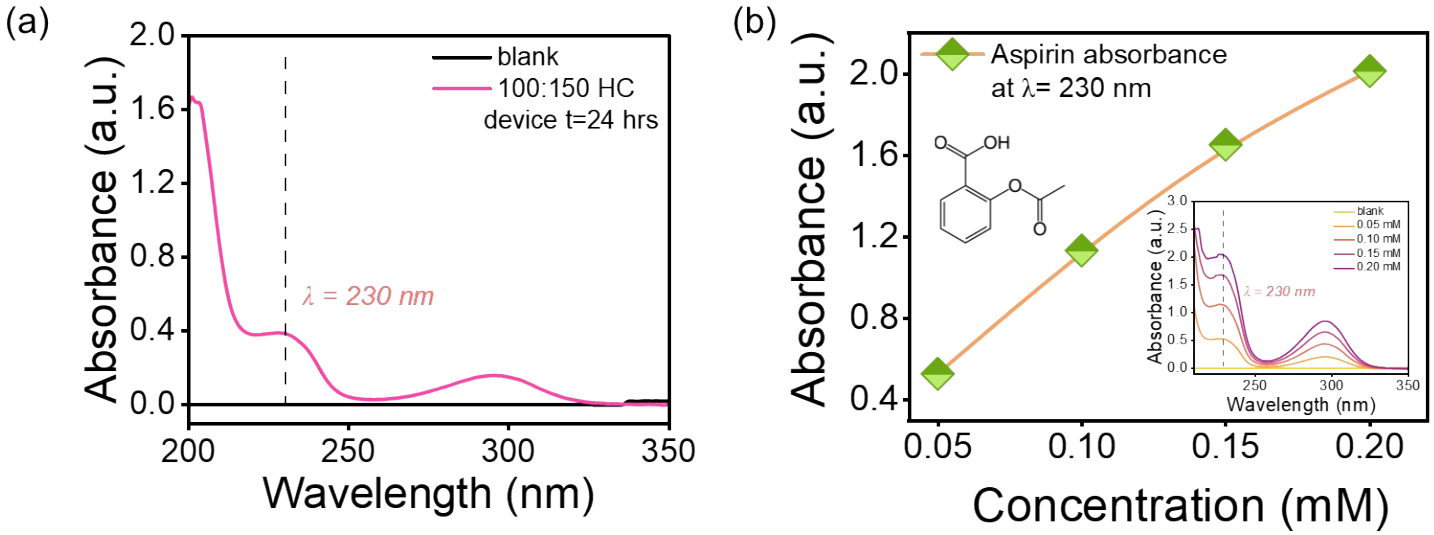

Figure S23: (a) UV-vis plot exhibiting absorbance for aspirin molecule in drain reservoir of IFM. (b) corresponding calibration plot at λ=230 nm.

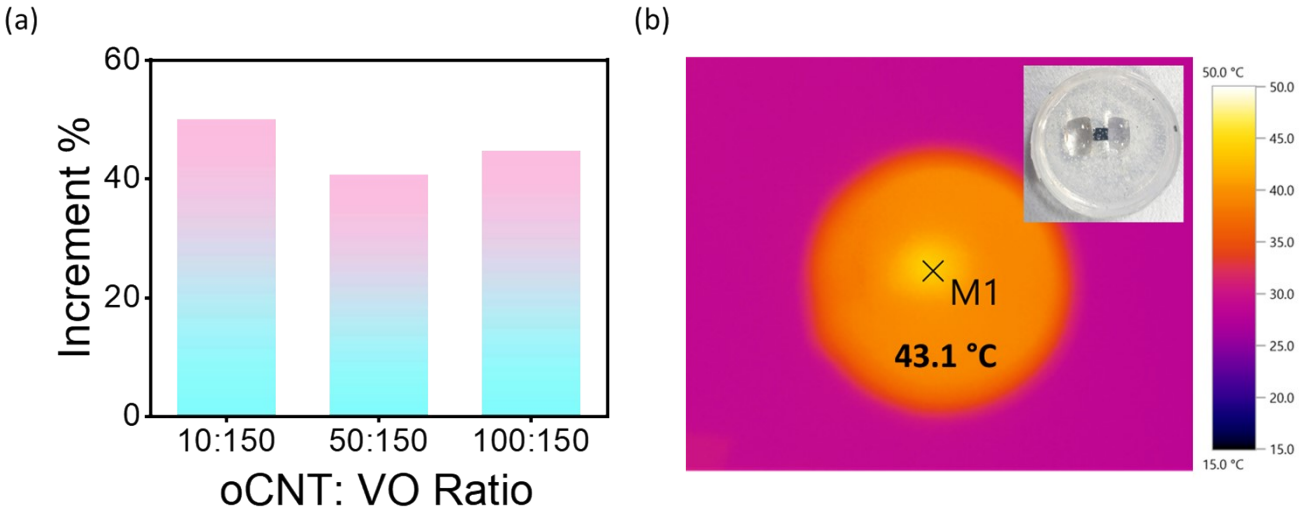

Figure S24: (a) The increment in Trp delivery upon light illumination on the IFM devices. (b) Thermal image of the IFM device along with a digital image in the subset.

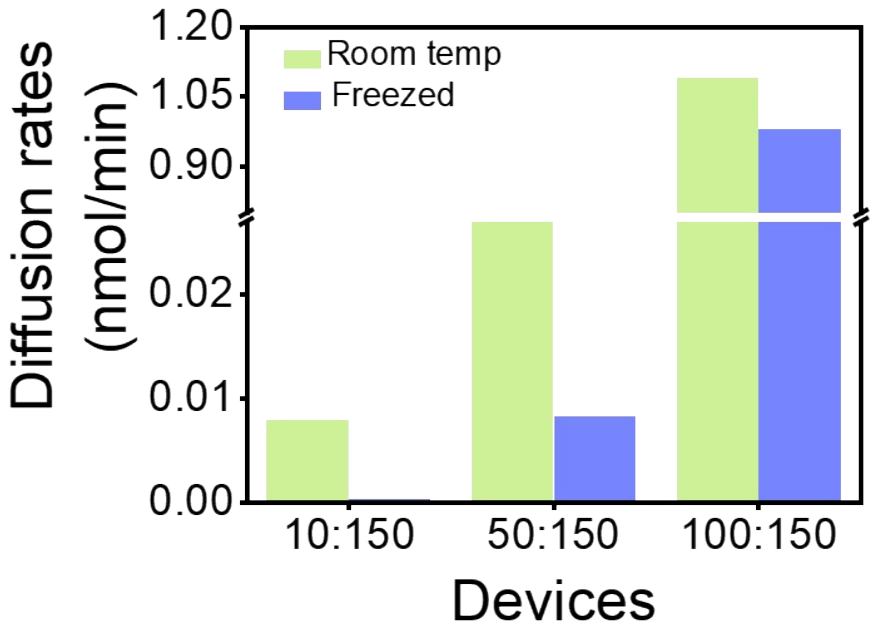

Figure S25: The decrease in delivery rates through IFM devices upon cooling.

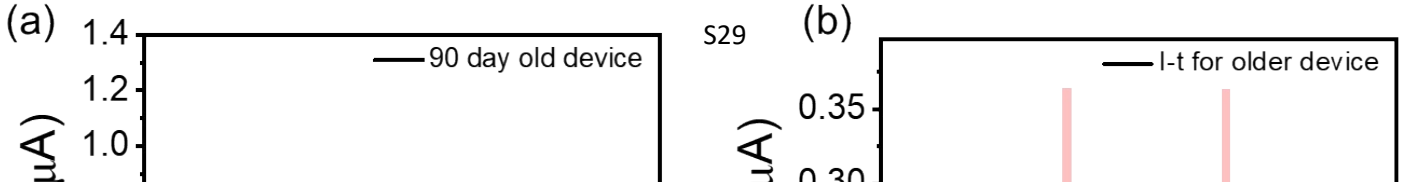

References:

1 C. Wang, D. Wang, W. Miao, L. Shi, S. Wang, Y. Tian and L. Jiang, *ACS Nano*, 2020, 14, 12614–12620.

2 J. Zhang, B. Liu, C. Chen, S. Jiang, Y. Zhang, B. Xu, A. Li, J. Xu, D. Wang, L. Zhang, Y. Hu, J. Li, D. Wu, J. Chu and Z. Shen, *ACS Appl. Mater. Interfaces*, 2022, 14, 35366–35375.

3 W. Xian, X. Xu, Y. Ge, Z. Xing, Z. Lai, Q.-W. Meng, Z. Dai, S. Wang, R. Chen, N. Huang, S. Ma and Q. Sun, *J. Am. Chem. Soc.*, 2024, 146, 33973–33982.

4 M. Tsutsui, W.-L. Hsu, C. Hsu, D. Garoli, S. Weng, H. Daiguji and T. Kawai, *Nat. Commun.*, 2025, 16, 1089.

5 J. Yang, X. Hu, X. Kong, P. Jia, D. Ji, D. Quan, L. Wang, Q. Wen, D. Lu, J. Wu, L. Jiang and W. Guo, *Nat. Commun.*, 2019, 10, 1171.